Spherical indentation of porous ceramics: Cracking and toughness

Zhangwei Chen [a,*], Xin Wang [b], Alan Atkinson [b], Nigel Brandon [a]

[a] Department of Earth Science and Engineering, Imperial College, London SW7 2BP, UK
[b] Department of Materials, Imperial College London SW7 2BP, UK

ARTICLE INFO

ABSTRACT

A combined experimental-numerical approach is used to characterise the fracture of a porous bulk ceramic material ($La_{0.6}Sr_{0.4}Co_{0.2}Fe_{0.8}O_3$) with porosities of 5–45%, undergoing spherical indentation. The Gurson model was used in FEM to describe the porosity densification. Indentation-induced radial cracks were observed, when the applied contact pressure exceeded threshold values, with no Hertzian ring-cone cracks found. FEM analysis indicated that the cracks propagated mainly during unloading, driven by the tensile hoop stress generated near the contact circle. The stress intensity at the crack tip was estimated using an approximate analysis of the FEM stress field to derive toughness values that were consistent with values determined by conventional methods, provided that the crack length is sufficiently large compared with the contact radius and can be measured accurately. The absence of ring-cone cracks during loading is due to the material's high modulus-to-hardness ratio and the small indenter radius as predicted by established theory.

1. Introduction

The development of porous ceramics is aimed at demanding engineering applications, such as insulation, filtering, catalysis, microelectronics, bioengineering and membranes [1–6]. Porous bulk ceramics are generally prepared by the partial sintering of powders at elevated temperatures. The influence of the resultant microstructure on typical elastic properties of such porous ceramics has been widely studied [7–12]. Although the property-microstructure correlation is complex in detail [13], the elastic and fracture properties depend mainly on the volume fraction of porosity [14].

Nanoindentation measurements, typically with the use of sharp indenters, have been extensively employed to characterise the mechanical properties (e.g. elastic modulus and hardness) of nominally dense materials [15,16]. However, the application of indentation to the mechanical characterisation of porous materials is not so common. This is because the presence of the porous microstructure brings added complexity to obtaining and interpreting reliable data. The complication arises from collapse and densification in the compressive field of the indenter, as observed in the indentation of highly porous silica foams [17] and ceramics [18]. Nevertheless, in previous studies we have used sharp indenters and

conventional methods (single edge-notched beam) to measure the fracture toughness of a typical porous ceramic used in solid oxide fuel cell (SOFC) technology and found that the two approaches gave results in acceptable agreement [19]. However, in many contact situations the contacting component does not have a sharp profile (like a sharp indenter), but is rather blunt and more like a spherical indenter. For example, in SOFC technology this might be the contact between a rib on a bipolar plate and the current collector layer of the cell. Therefore it is important to understand contact damage when a blunt (spherical) indenter is loaded into a porous ceramic.

In an earlier paper from this study, the influence of porosity on the elastic and plastic properties deduced from spherical indentation of a typical porous ceramic was investigated [20]. The interpretation was based on finite element modelling of the indentation employing the Gurson model [21] to describe the collapse and densification of the porous structure in the compressive plastic zone under the indenter. In the present paper we extend this approach to investigate indentation-induced cracking of the same porous ceramics when higher contact pressures are applied.

Very few studies are reported in the literature regarding spherical indentation-induced damage in porous ceramics. For example, Latella et al. [22] studied contact damage in porous and dense liquid-phase-sintered alumina using large spherical indenters. Their results showed that in the low porosity specimens (2.5% porosity) the spherical contact induced classical Hertzian ring and cone cracks penetrating below the surface with no detectable residual surface depression caused by the indenter, indicating negligible

Table 1
Properties of LSCF specimens and thresholds for radial cracking.

Sintering Temperature (°C)	Porosity (%)	Threshold Load (mN)	Threshold Depth (μm)	Threshold Pressure (GPa)	E below Threshold (GPa)	E above Threshold (GPa)
900	44.9 ± 0.3	600	5.33	0.88 ± 0.03	33.4 ± 1.2	28.9 ± 1.2
1000	36.3 ± 1.1	800	5.31	1.16 ± 0.06	52.7 ± 3.7	47.4 ± 2.3
1100	28.7 ± 0.9	2000	5.01	3.28 ± 0.59	86.8 ± 3.1	84.1 ± 2.0
1200	5.2 ± 0.1	800	1.03	7.01 ± 0.21	178.2 ± 2.3	162.9 ± 2.2

plastic deformation. Increasing porosity (up to 17.8%) induced a transition to a quasi-plastic response in which there was collapse of the porous material and formation of surface ring cracks in the indented region that did not penetrate appreciably below the surface. No radial cracks were seen in any specimen.

In the current study, spherical indentation at a wide range of loads was carried out to generate cracks in the porous ceramic material $La_{0.6}Sr_{0.4}Co_{0.2}Fe_{0.8}O_{3-\delta}$ (LSCF), which was sintered from powder at different temperatures between 900 and 1200 °C, resulting in pore fractions between 45 and 5%. Contrary to the behaviour of alumina observed by Latella et al. [22] indentation-induced radial cracks were observed above a threshold contact pressure and their geometry was characterised using FIB-SEM. Numerical analysis (FEM) was performed to determine the stress field in the absence of cracks during both loading and unloading; using the Gurson model to describe the collapse and densification of the porous material. This stress field, together with the dimensions of the cracks observed experimentally, was then used to estimate the fracture toughness of the porous material. Finally, the values of fracture toughness obtained in this way were compared with values obtained using sharp indenter (Berkovich) and notched beam methods.

2. Experiments and simulations

2.1. Indentation tests

The perovskite material $La_{0.6}Sr_{0.4}Co_{0.2}Fe_{0.8}O_{3-\delta}$ (LSCF) is used widely as a porous cathode in solid oxide fuel cells (SOFCs). Bulk LSCF specimens with different porosities were prepared by sintering LSCF powders at different temperatures. The sintering temperatures and the corresponding percentage porosities are shown in Table 1. Indentation experiments over the load range 50–10000 mN were carried out using a spherical diamond indenter (radius 25 μm). Table 1 also shows the values of critical load, indentation pressure and depth of indentation when cracking was first observed (by microscopic examination after unloading). The apparent elastic modulus (derived in the standard way from the unloading stiffness) was calculated for maximum indentation loads below and above the critical load and the results are also displayed in Table 1. They show a small, but significant, reduction at loads above the critical value indicating that cracking has reduced the local stiffness in the neighbourhood of the indentation. Focused ion beam-scanning electron microscopy (FIB-SEM) was used to study the surface and cross-sectional microstructures of the specimens before and after indentation. Details of the specimen preparation, indentation and FIB-SEM procedure can be found in [18]. Technical aspects of the indentation process are fully described in [18] and [20].

2.2. Finite element modelling

Axisymmetric finite element simulation of the indentation process, taking into account the collapse and densification of the porous material under the indenter, was developed in the earlier part of the current study [20]. That work showed that the Gurson
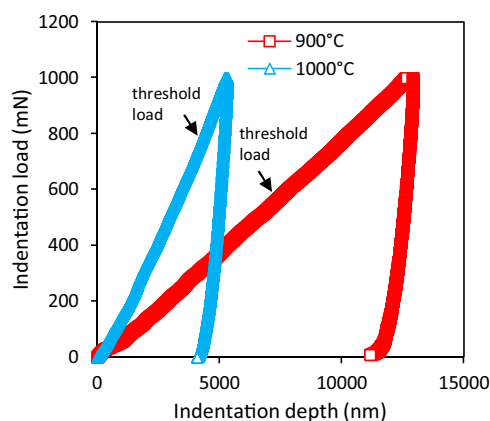

Fig. 1. Experimental indentation load-depth curves generated at 1000 mN load (beyond each corresponding threshold load) for LSCF bulk specimens sintered at 900 °C and 1000 °C.

model could provide a suitable description of densification in the "plastic zone" of the indentation, despite the fact that the Gurson model is normally applied to plastic deformation of porous metals and is only strictly valid when the porosity is lower than approximately 10%. As a result, although application of the Gurson model in the present study describes the densification behaviour acceptably, the critical materials parameter used in the Gurson model (the yield stress of the fully dense material) has no fundamental significance and is regarded as an adjustable parameter whose value is determined by fitting to the experimental indentation curve. In the present study, FE simulations were carried out using Abaqus CAE 6.12 (Dassault Systemes, USA) for indentation loads (or the corresponding indentation depths) equal to, or greater than, the threshold values that were observed to trigger the radial cracks found in the indentation experiments. The full description and implementation of the models can be found in our earlier paper [20].

3. Results and discussion

3.1. Crack characterisation

The LSCF specimens were subjected to spherical indentation at a series of loads ranging from 50 to 10000 mN. In addition to the densification deformation (regarded as the permanent plastic deformation) resulting from crushing of the particle-pore networks under indentation, as described in [20], indentation-induced radial cracks were also found in the specimens when the applied load surpassed a threshold value, determined by microscopic characterisation after indentation. Below the threshold loads, permanent "pseudo plastic" deformation without any radial cracks was observed in all samples.

Some typical experimental indentation curves are shown in Fig. 1. In general, the loading-unloading curves did not show any obvious evidence of long-range fracture events (such as clear pop-in responses), and therefore microscopic inspection of the specimens was required to detect whether any fracture had

Table 2
Specimen properties and condition for cone cracking.

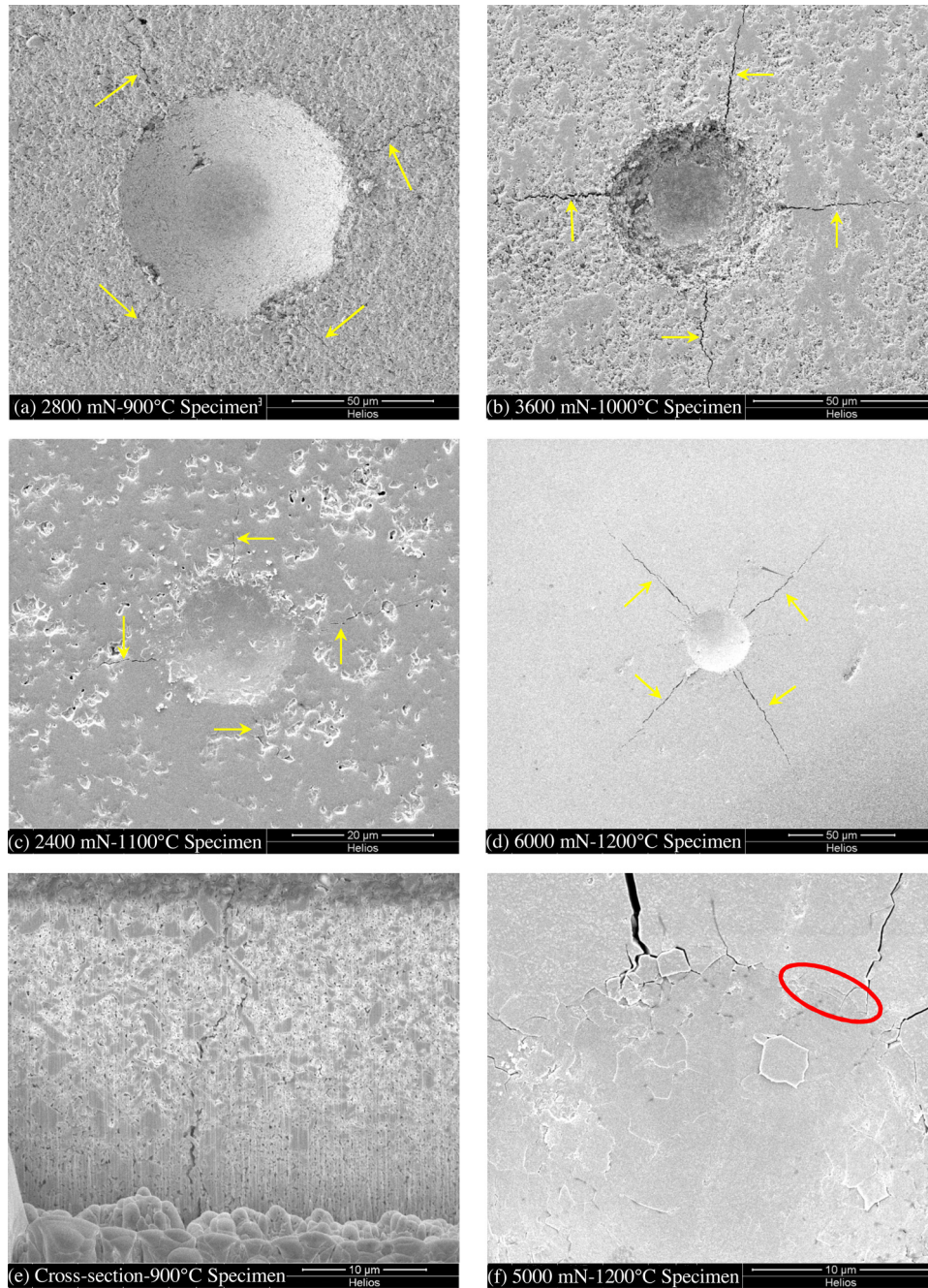| Sintering temperature (°C)	E (GPa)	H_B (GPa)	K_{Ic} (MPa m$^{1/2}$)	Γ (J m^{-2})	p_m^*/H
900	33.4	0.57	0.57	8.9	20.6
1000	52.7	0.81	0.68	8.0	19.0
1100	86.8	2.26	0.74	5.7	8.5
1200	178	6.12	1.13	6.5	5.3

Fig. 2. Radial cracks in the specimens (with arrows showing cracks): (a) 900 °C-specimen after 2800 mN indentation, (b) 1000 °C-specimen after 3600 mN indentation, (c) 1100 °C-specimen after 2400 mN indentation, (d) 1200 °C-specimen after 6000 mN indentation. (e) is a cross-sectional view outside the contact circle of the 900 °C-specimen after 2800 mN indentation, showing no ring-cone cracks but a radial crack penetrating downward, (f) magnified view of a 1200 °C-specimen surface after 5000 mN indentation showing possible fragmented ring cracks and coarse grains surrounded by micro-cracks at the boundary of the contact circle.

occurred. The FIB-SEM slice and view technique (described in [18]) was applied to study the microstructures in the plastically deformed regions, and cracking of the material immediately underneath and in the vicinity of the indented areas.

Studies [23–25] of the spherical indentation of brittle dense materials, including glass, silicon, alumina and other ceramics, often show distinct cone cracks penetrating into the bulk, developing from ring cracks initiated on the contact area surface. Cone
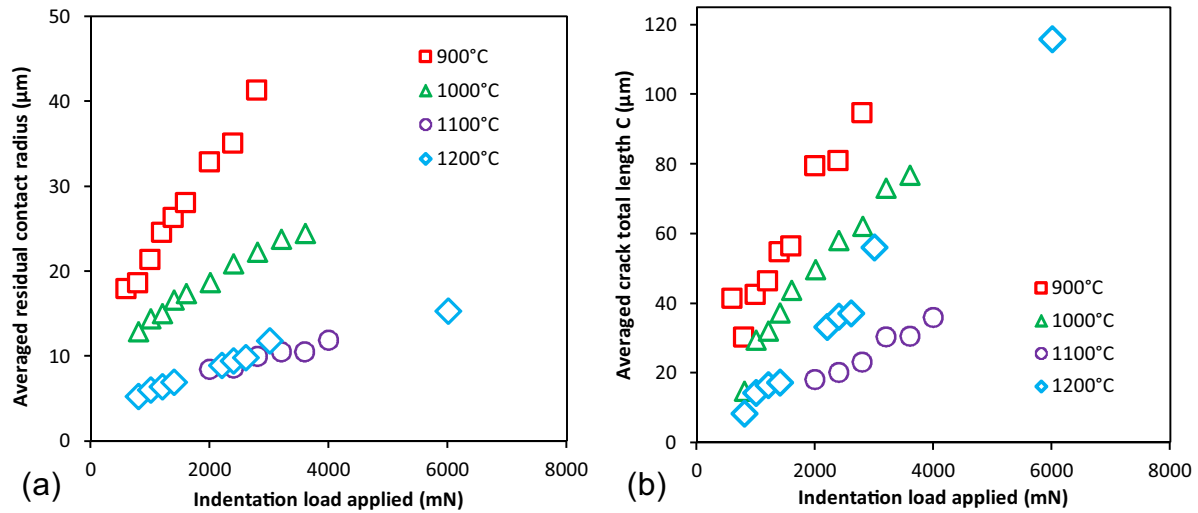
Fig. 3. Measured crack dimensions: (a) averaged residual contact radius, (b) averaged total crack length *c* measured from the contact centre to the crack tip.

crack formation is experimentally well documented and theoretically well understood. Cone cracks nucleate first as ring cracks at the material surface from flaws just outside the contact circle, and then propagate as truncated cone cracks on further loading. In order to produce a cone crack the indentation contact must be elastic (negligible plastic deformation). Evans and Wilshaw [26] studied and analysed cracking induced by spherical indentation in a range of dense ceramic materials. They found that there is an interaction between plastic deformation and cracking behaviour that depends on the radius of the indenter. Above a critical radius Hertzian ring and cone cracks are formed before the onset of plastic deformation. For indenters with radius below the critical value, plastic deformation substantially modifies the stress field such that the conditions for ring and cone cracking are not met and a system of radial and sub-surface lateral cracks is formed.

In the current study, microscopic observations of the residual indents (such as shown in Fig. 2) revealed significant radial cracks on the surface of the specimens, when indented above the critical loads. No ring and cone cracks were observed, nor was there any evidence of sub-surface lateral cracks of the type described by Evans and Wilshaw. The conditions for the formation of ring and cone cracks have been analysed in detail by Frank and Lawn [27]. They conclude that a penetrating cone crack will be formed at a critical load P^* given by,

$$P^* = 1.17 \times 10^5 k \Gamma R \tag{1}$$

where Γ is the fracture energy (twice the surface energy for ideal brittle fracture), R is the indenter radius (25 μm in the present study) and k is given by,

$$k = \frac{9}{16}\left((1-\nu^2) + \frac{(1-\nu_i^2)E}{E_i}\right) \tag{2}$$

In this equation E and ν are Young's modulus and Poisson's ratio, and the subscript indicates the indenter material.

Inserting measured values of the required parameters from Table 2 into these equations (assuming a perfectly rigid indenter) gives a critical load for the LSCF sintered at 1200 °C of 9.8 N which is required to produce ring and cone cracking. This is much greater than the threshold load of 0.8 N (Table 1) observed to initiate radial cracking in this specimen. Thus the critical load for ring and cone cracking cannot be reached without generating radial cracks. An alternative way of describing this is to compare the critical mean contact pressure with the hardness bearing in mind that plastic

deformation first initiates at the central point under the spherical indenter when the mean contact pressure is approximately equal to the plastic hardness. The mean contact pressure $p_m = P/(\pi a^2)$ where a is the contact radius and, for a perfectly elastic contact, is given by,

$$a^3 = \frac{4}{3}\frac{kPR}{E} \tag{3}$$

Hence,

$$\left(\frac{p_m^*}{H}\right)^3 = \frac{1.17 \times 10^5 \Gamma}{kR}\left(\frac{9}{16\pi^3}\right)\frac{E^2}{H^3} \tag{4}$$

The ratio p_m^*/H is evaluated in Table 2 for the LSCF specimens using the experimentally determined parameters listed in Table 2. (H_B is the hardness measured using a sharp indenter; in this case a Berkovich indenter.) The results in Table 2 show that in all cases the mean pressure required to produce cone cracks is much greater than the hardness and therefore the specimens undergo extensive plastic deformation thereby preventing the condition for cone cracking to be reached with a sphere of the radius used here. Since p_m^*/H is proportional to $R^{-1/3}$ much larger spheres would be required to produce cone cracks.

In this study, on the surface of the specimens only radial cracks were seen. The cross-sectional observations (such as Fig. 2(e)) showed that the radial cracks penetrated into the porous LSCF specimens, consistent with a system of centre-loaded radial penny-shaped cracks. No evidence was found of any ring and cone cracks or lateral cracks in the cross sections. However, the specimen sintered at 1200 °C and indented at 5000 mN shown in Fig. 2 (f) does display a more complicated cracking behaviour with a possible ring crack at the circumference of the indented area in addition to the radial cracks. Also it was found that the spherical indentation generally generated four radial cracks visible on the surface, at approximately 90° intervals, even though the indenter had no sharp edges to initiate cracks (as is the case for Berkovich or Vickers indenters). The radial cracks are caused by a tangential tensile hoop stress and this will be partially relieved by the formation of the first crack (visible as a pair of half-cracks on the surface). The stress relief will be least perpendicular to the first crack thereby permitting nucleation of a second crack perpendicular to the first one at a slightly higher load. The complete absence of radial cracks reported by Guiberteau et al. [28] for alumina specimens undergoing spherical indentation can be attributed to the relatively small plastic deformation (which is the major driving force for radial crack growth) compared to elastic
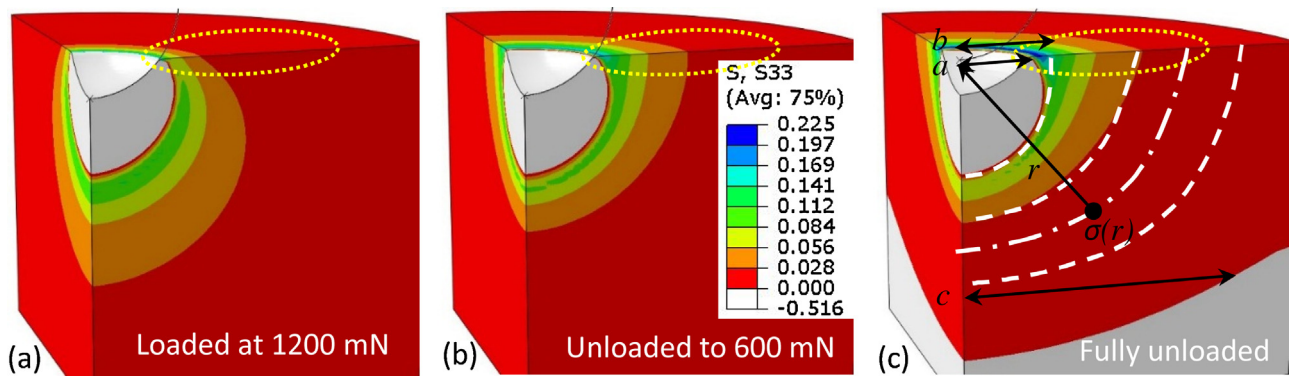
Fig. 4. Contour plots showing evolution of the hoop stress (S_{33} in GPa) during a simulated indentation cycle to 1200 mN maximum load (twice the threshold load), for the specimen sintered at 900 °C, (a) fully loaded at 1200 mN, (b) on unloading back to 600 mN, (c) after full unloading. Compressive stress is shown negative and tensile stress is shown positive. Here, all the regions of compressive stress are shown in grey for clarity. The dashed ellipse encompasses the surface region where radial cracks were observed experimentally. Also shown in (c) are the schematic and variables used for numerical calculation of toughness described in the later section (with *a* being the residual contact radius, *b* the radius of the plastic zone inside which the hoop stresses are compressive, *c* the radius of crack, and $\sigma(r)$ is the hoop stress S_{33} (in GPa) at a radial distance *r*).
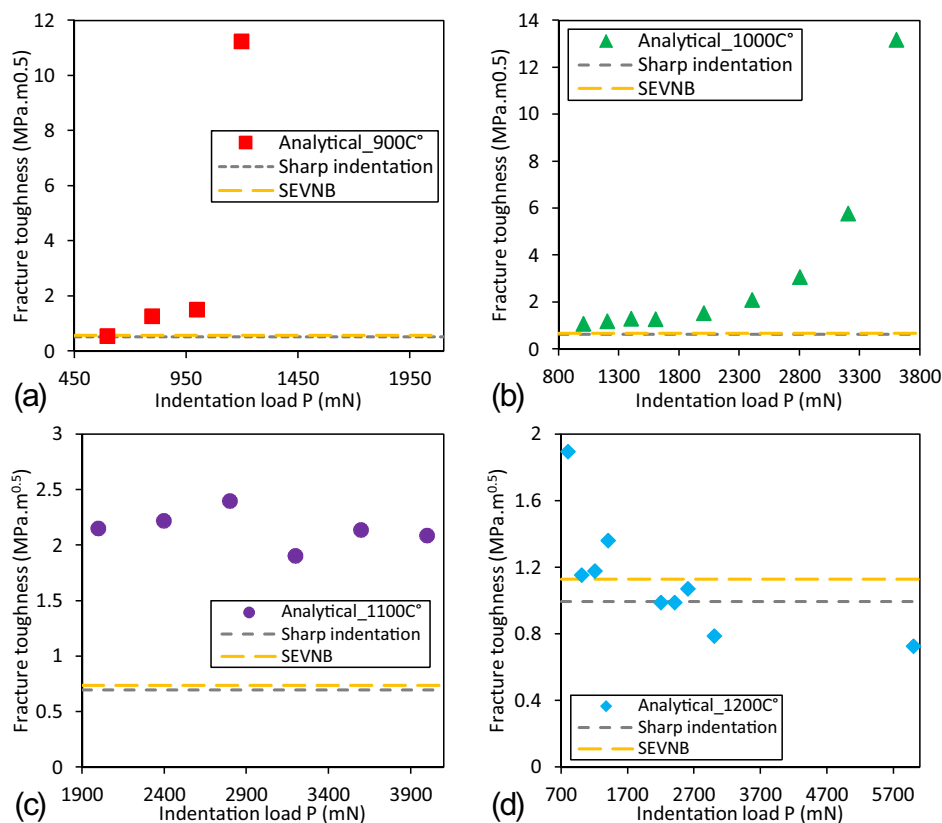

Fig. 5. Fracture toughness estimated using an analytical method and compared with values measured using Berkovich sharp indentation and SEVNB experiments [19] for specimens sintered at different temperatures. (a) 900 °C specimen, (b) 1000 °C specimen, (c) 1100 °C specimen and (d) 1200 °C specimen.

deformation. This is due to the higher hardness of alumina and their use of much larger spheres with radii between 1.98 and 12.7 mm.

The resulting crack dimensions on the specimen surface were measured after indentation using SEM and the results are plotted in Fig. 3. The total crack length in Fig. 3 is the length of the crack on the surface measured from the centre of the contact circle. In Fig. 3 (a) it can be seen that after loads were increased above 1200 mN, the average residual contact radii for the specimens sintered at 900 °C exceeded 25 μm, which is the radius of the indenter tip. It is possible for this to occur because the indenter is not a sphere, but is actually a hemi-spherical diamond attached to a truncated conical metal stub. Therefore, the experiments in which the contact radius exceeded 25 μm were omitted from subsequent analysis. It is also interesting

that, for the specimens sintered at 1200 °C, cracks started to appear at loads as low as 800 mN, which is much smaller than the threshold loads for the more porous specimens sintered at lower temperatures. However, the threshold mean contact pressure (Table 1) is seen to increase monotonically as the density increases and thus the lower threshold load for the densest specimen is a consequence of its greater hardness and modulus and lack of densification of porosity under compression. Similarly, larger crack sizes were generated in the specimens sintered at 1200 °C than were observed in the specimens sintered at 1100 °C indented at the same load. This is also a consequence of the lack of densification under compression and does not indicate a lowering of toughness, as discussed in more detail later.
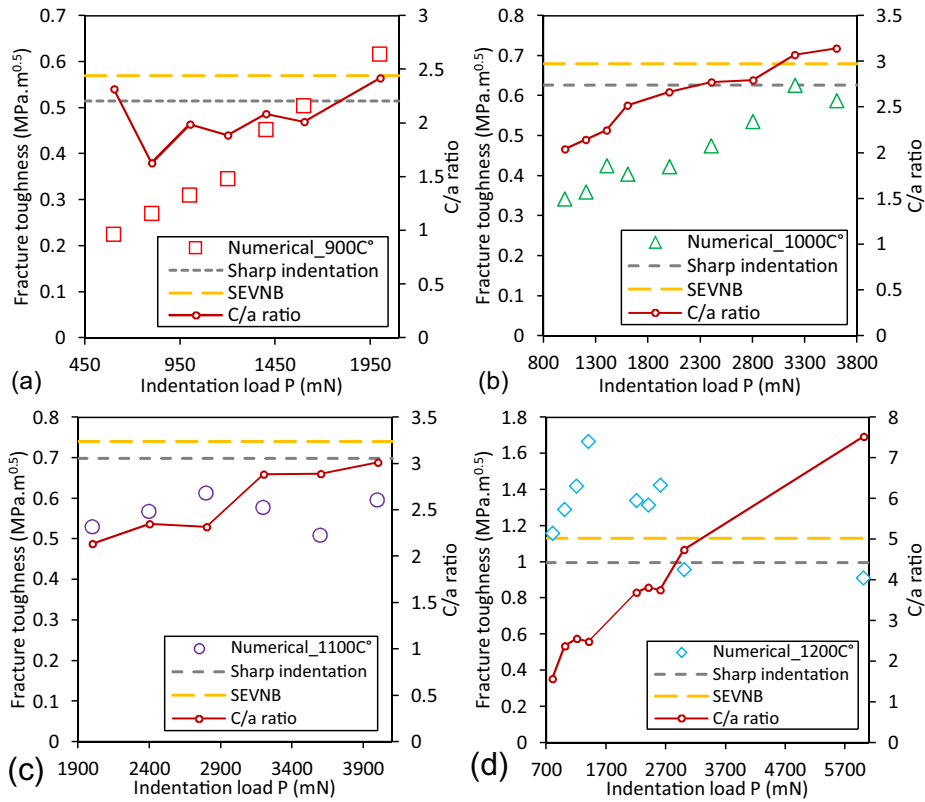
Fig. 6. Fracture toughness and c/a ratio for the specimens sintered at different temperatures, (a) 900 °C specimen, (b) 1000 °C specimen, (c) 1100 °C specimen and (d) 1200 °C specimen.

3.2. Stress analysis

As mentioned earlier, the hoop stress (S_{33}) normal to model plane is responsible for the initiation and propagation of radial cracks. Fig. 4 shows the contour plots of S_{33} in the history of loading and unloading steps during indenting to twice the critical load (1200 mN) for the simulation corresponding to the specimen sintered at 900 °C.

The FEM model is described in cylindrical coordinates r, z, and θ. The radial and axial coordinates of a point on the original 2D model plane are denoted by r and z, respectively, and coincide with conventional Cartesian coordinates in this plane. Therefore the cylindrical radial stress S_{rr} is the same as the Cartesian S_{11}, the axial stress S_{zz} is S_{22}, and the hoop stress $S_{\theta\theta}$ is S_{33}.

As can be seen in Fig. 4, the tensile hoop stress near the surface region (encompassed in the dashed ellipse) close to the contact area is relatively low and has short range at the maximum load. However it increases in both magnitude and spatial extent due to the elastic relaxation of the deformed material when unloading takes place. The FEM results thus show that the radial cracks intersecting the surface propagate mainly during the unloading step when the region of tensile hoop stress expands. However, they could have initiated in the tensile hoop stress below the surface during loading as in Fig. 4 (a).

3.3. Estimation of fracture toughness

In this study, both an analytical approach and a numerical method are explored to calculate the fracture toughness of the specimens which displayed radial cracking in order to quantify the fracture process.

3.3.1. Fracture toughness estimated using analytical method

According to Lawn et al. [29], radial crack growth is due to a residual field after unloading arising from plastic deformation underneath the indenter. An analytical formula (Eq. (5)) was derived in [29] for evaluating the stress intensity factor for a pyramidal indenter:

$$K_{Ic} = \S \left(\frac{E}{H}\right)^{1-m} \left(\cot\psi\right)^{\frac{2}{3}} \frac{P}{c^{3/2}} \tag{5}$$

where E and H are elastic modulus and hardness, P is the load and c is crack length. m and $\S$ are constants which can be taken as 0.5 and 0.032 respectively. 2ψ is the angle between the pyramid faces and defines the strain in the material in contact with the indenter.

We modified this approach by adapting it to the strain generated by a spherical indenter resulting in (Eq. (6)) for a spherical indenter:

$$K_{Ic} = \S \left(\frac{E}{H}\right)^{1-m} \left(\frac{\pi}{12}\right)^{\frac{2}{3}} \left[3\tan\left(\frac{\phi}{2}\right) + \tan^2\left(\frac{\phi}{2}\right)\right]^{\frac{2}{3}} \frac{P}{c^{3/2}} \tag{6}$$

where, $m = 0.5$ and $\S = 0.032$, $\phi = \text{asin}\left(\frac{a}{R}\right)$, with a being the radius of the contact circle and R the radius of the spherical indenter.

K_{Ic} values calculated using Eq. (6) are plotted in Fig. 5 as a function of maximum indentation load for each of the specimens and compared with the results derived from other methods, i.e. the Berkovich sharp indentation and the Single-Edge V-Notched Beam (SEVNB) methods [19]. For the nominally dense specimens (which were sintered at 1200 °C), the K_{Ic} values are reasonably close to those measured by other methods. However, it is clear that, for the porous LSCF specimens, the K_{Ic} values calculated using Eq. (6) are significantly larger than those measured using the other methods, which themselves are in good agreement. An important assumption underpinning Eqs. (5) and (6) is that the material volume is not changed during plastic deformation (i.e. constant volume assumption). For a dense ceramic material this assumption is valid.

However, the assumption is no longer valid for porous ceramics due to the crushing and densification of the particle-pore networks underneath the indenter. The constant volume assumption would lead to an overestimation of the plastic zone size and hence the residual field leading to an overestimation of K_{Ic}. The question then arises regarding why the Berkovich sharp indentation gives values of K_{Ic} in good agreement with those from the SEVNB method even though there is still collapse and densification under the sharp indenter. This is currently not understood and is probably fortuitous.

3.3.2. Fracture toughness estimated using numerical method

Given the inadequacy of the analytical approach described above, we have used a numerical approach that explicitly takes into account the densification in the plastic zone and is quantified in the FE simulations.

Based on the work of Lawn et al. [29], the opening mode stress intensity K_I for a half-penny (semi-circular) crack induced by indentation and subjected to normal stresses distributed over the crack faces can be expressed by Eq. (7),

$$K_I = \left(\frac{2}{c}\right)^{0.5} \int_b^c \frac{r\sigma(r)\,dr}{\sqrt{c^2 - r^2}} \tag{7}$$

In this expression b is the radius of the plastic zone inside which the hoop stresses are compressive and c the radius of crack (i.e. the crack length measured from the contact centre). $\sigma(r)$ is the hoop stress, S_{33}, after fully unloading in the absence of the crack, at radial distance r from the centre of the contact on the original surface. The geometry is illustrated in Fig. 4 (c). Eq. (7) is based on the known solution for the stress intensity at the tip of a circular crack subjected to a point load applied at its centre. For indentation the point load is approximated as the displacement caused by the irreversible deformation of the plastic zone. Thus a necessary condition for Eq. (7) to be valid is that the crack length should be much greater than the plastic zone radius, $c \gg b \approx a$.

FE simulations were carried out using Abaqus with loads (or equivalent indentation depths) corresponding to those shown in Fig. 3 for the different specimens. The hoop stress contours (e.g. as shown in Fig. 4 (c) absent any crack) are approximately semi-circular in shape and therefore the stress distribution is suitable for application of Eq. (7).

After each simulation was completed, circular paths with varying radius $b \leq r \leq c$ were created to calculate the averaged hoop stress $\sigma(r)$ over each path. In this calculation b was taken as the radius of the plastic zone deduced from the FE simulation, whereas c was taken as the experimentally observed crack length for the given maximum indenter load. The values of the averaged hoop stress $\sigma(r)$ were plotted as a function of the radial distance r, followed by polynomial fitting in the form $B + \sum A_n r^n$, where B and A_n are a constant and coefficients of variables, respectively. The fitted continuous function was then substituted into Eq. (7) to compute the integral and hence the corresponding K was calculated as a function of the maximum indentation load and the results are shown in Fig. 6 together with the corresponding ratio of crack length to residual contact radius, a, (contact radius at maximum load) which is approximately equal to the plastic zone radius. It can be seen in Fig. 6 that there is a significant increase in calculated toughness with indentation load for the specimens sintered at 900 and 1000 °C, but not for the specimens sintered at 1100 and 1200 °C. This is probably partly due to difficulty in measuring the crack length of short cracks, particularly in the porous materials. The experimental crack length not only appears in the measured ratio c/a, but also as an input parameter in the calculation of toughness through the upper limit of integration in Eq. (7). In addition, Eq.

(7) is only a reasonable approximation when $c \gg a$ which introduces additional errors when the cracks are short. Also shown in Fig. 6 are the toughness values measured using the Berkovich indentation and the SEVNB methods [19] for comparison. In general the fracture toughness values derived by the numerical approach at the higher loads tend to generate toughness values much closer to the values measured by the other methods.

From Fig. 3 it is seen that for the specimen sintered at 1200 °C the measured crack lengths deviated from expected sequence exhibited by the specimens sintered at lower temperatures. Nevertheless, the toughness results in Fig. 6 remained consistent with the trend of toughness increasing as porosity decreases. The reason for this apparent discrepancy is that the toughness also depends of the elastic modulus and hardness in addition to the crack length.

4. Conclusions

In this study, a combined experimental and numerical approach has been used to analyse cracking phenomena in porous bulk LSCF ceramics induced by spherical indentation. It was observed experimentally that radial cracks were generated in all specimens, with porosity ranging from 5 to 45%, above a threshold indentation pressure which varied with porosity. No Hertzian ring-cone cracks were observed in any of the current experiments

Finite element simulation, including collapse and densification of the porous structure in the compressive field of the indenter during loading, shows that a tensile hoop stress field develops on loading and increases and expands on unloading to generate the radial cracks. The absence of Hertzian ring-cone cracks is partly due to the small radius of the indenter and partly due to the relatively low hardness of these materials. Both these result in significant plastic deformation before the critical load required to produce cone cracks is reached.

Adaptation of the standard theory for indentation toughness, using sharp indenters, to the geometry of a spherical indenter does not give accurate values for fracture toughness of the more porous specimens. This is because the standard theory assumes conservation of volume during plastic deformation which is not valid in porous specimens. Since this also applies when using a sharp indenter, it is unclear why the sharp indenter appears to give accurate toughness results.

The fracture toughness was calculated from the FE post loading hoop stress field (in the absence of a crack and including the densification under the loaded indenter) using an approximate analysis for the crack tip stress intensity in this field. The resulting toughness was in acceptable agreement with values measured by other methods (sharp indenter and notched beam) provided that the loads were sufficiently high to generate cracks of a length that could be accurately measured and was greater than a few times the radius of the contact circle.

The Gurson model is useful for simulating the effect of densification when assessing contact damage in porous ceramics.

Appendix A. Supplementary data

Raw data on which this paper is based can be openly accessed at https://dx.doi.org/10.6084/m9.figshare.2114305.v1

Supplementary data associated with this article can be found, in the online version, at http://dx.doi.org/10.1016/j.jeurceramsoc.2016.05.010.

References

[1] Z. Chen, C. Lu, Humidity sensors: a review of materials and mechanisms, Sens. Lett. 3 (4) (2005) 274–295.

[2] T. Shimizu, K. Matsuura, H. Furue, K. Matsuzak, Thermal conductivity of high porosity alumina refractory bricks made by a slurry gelation and foaming method, J. Eur. Ceram. Soc. 33 (15) (2013) 3429–3435.

[3] C.W. Tanner, K.-Z. Fung, A.V. Virkar, The effect of porous composite electrode structure on solid oxide fuel cell performance, J. Electrochem. Soc. 144 (1) (1997) 21–30.

[4] T. Thamaraiselvi, S. Rajeswari, Biological evaluation of bioceramic materials-a review, Carbon 24 (31) (2004) 172.

[5] J. Adler, Ceramic diesel particulate filters, Int. J. Appl. Ceram. Technol. 2 (6) (2005) 429–439.

[6] N. Brandon, D. Brett, Engineering porous materials for fuel cell applications, Philos. Trans. R. Soc. A Math. Phys. Eng. Sci. 364 (1838) (2006) 147–159.

[7] R.W. Rice, Porosity of Ceramics: Properties and Applications, CRC Press, 1998.

[8] R. Coble, W. Kingery, Effect of porosity on physical properties of sintered alumina, J. Am. Ceram. Soc. 39 (11) (1956) 377–385.

[9] E.A. Dean, J.A. Lopez, Empirical dependence of elastic moduli on porosity for ceramic materials, J. Am. Ceram. Soc. 66 (5) (1983) 366–370.

[10] C. Herakovich, S. Baxter, Influence of pore geometry on the effective response of porous media, J. Mater. Sci. 34 (7) (1999) 1595–1609.

[11] D. Hardy, D.J. Green, Mechanical properties of a partially sintered alumina, J. Eur. Ceram. Soc. 15 (8) (1995) 769–775.

[12] D.J. Green, C. Nader, R. Brezny, Elastic behaviour of partially-sintered alumina, in: Sintering of Advanced Ceramics Proc Symposium on Sintering of Advanced Ceramics Cincinnati, Ohio, 2–5 May 1988, 1988, pp. 345–356.

[13] R. Rice, Porosity of Ceramics, Marcel Dekker, New York, 1998.

[14] Z. Chen, X. Wang, F. Giuliani, A. Atkinson, Microstructural characteristics and elastic modulus of porous solids, Acta Mater. 89 (2015) 268–277.

[15] W.C. Oliver, G.M. Pharr, An improved technique for determining hardness and elastic modulus using load and displacement sensing indentation experiments, J. Mater. Res. 7 (6) (1992) 1564–1583.

[16] A.C. Fischer-Cripps, Nanoindentation, 3rd edn, Springer, New York, 2011.

[17] Y. Toivola, A. Stein, R.F. Cook, Depth-sensing indentation response of ordered silica foam, J. Mater. Res. 19 (01) (2004) 260–271.

[18] Z. Chen, X. Wang, V. Bhakhri, F. Giuliani, A. Atkinson, Nanoindentation of porous bulk and thin films of La0.6Sr0.4Co0.2Fe0.8O3-δ, Acta Mater. 61 (15) (2013) 5720–5734.

[19] Z. Chen, X. Wang, F. Giuliani, A. Atkinson, Fracture toughness of porous material of LSCF in bulk and film forms, J. Am. Ceram. Soc. 98 (7) (2015) 2183–2190.

[20] Z. Chen, X. Wang, A. Atkinson, N. Brandon, Spherical indentation of porous ceramics: elasticity and hardness, J. Eur. Ceram. Soc. 36 (6) (2016) 1435–1445.

[21] A.L. Gurson, Continuum theory of ductile rupture by void nucleation and growth: part I—Yield criteria and flow rules for porous ductile media, J. Eng. Mater. Technol. 99 (1) (1977) 2–15.

[22] B.A. Latella, B.H. O.Connor, N.P. Padture, B.R. Lawn, Hertzian contact damage in porous alumina ceramics, J. Am. Ceram. Soc. 80 (4) (1997) 1027–1031.

[23] J.T. Hagan, M.V. Swain, The origin of median and lateral cracks around plastic indents in brittle materials, J. Phys. D Appl. Phys. 11 (15) (1978) 2091.

[24] B.R. Lawn, Indentation of ceramics with spheres: a century after Hertz, J. Am. Ceram. Soc. 81 (8) (1998) 1977–1994.

[25] Y. Zhang, I. Sailer, B.R. Lawn, Fatigue of dental ceramics, J. Dent. 41 (12) (2013) 1135–1147.

[26] A.G. Evans, T.R. Wilshaw, Quasi-static solid particle damage in brittle solids—I: Observations analysis and implications, Acta Metall. 24 (10) (1976) 939–956.

[27] F. Frank, B. Lawn, On the theory of Hertzian fracture, Proc. R. Soc. Lond. Ser. A Math. Phys. Sci. 299 (1458) (1967) 291–306.

[28] F. Guiberteau, N.P. Padture, B.R. Lawn, Effect of grain size on Hertzian contact damage in alumina, J. Am. Ceram. Soc. 77 (7) (1994) 1825–1831.

[29] B. Lawn, A. Evans, D. Marshall, Elastic/plastic indentation damage in ceramics: the median/radial cracks system, J. Am. Ceram. Soc. 63 (1980) 574.